Water-in-Salt Electrolytes for Reversible Zinc Electrodeposition for Dynamic Windows

Journal of The Electrochemical Society, 2023 **170** 112502
1945-7111/2023/170(11)/112502/8/$40.00 © 2023 The Electrochemical Society ("ECS"). Published on behalf of ECS by IOP Publishing Limited

Water-in-Salt Electrolytes for Reversible Zinc Electrodeposition for Dynamic Windows

Desmond C. Madu, Andrew A. Thompson, Madeline J. Leahy, Micah V. Lilo, and Christopher J. Barile[z]

Department of Chemistry, University of Nevada, Reno, Nevada 89557, United States of America

Reversible metal electrodeposition (RME) is an emerging and promising method for designing dynamic windows with electrically controllable transmission, excellent color neutrality, and wide dynamic range. Despite its very negative deposition voltage, Zn is a viable option for metal-based dynamic windows due to its fast switching kinetics and reversibility. In this manuscript, we describe the construction of Zn RME dynamic windows using water-in-salt electrolytes (WISe). By systematically comparing different electrolytes, we study the effects of different WISe components on Zn RME spectroelectrochemistry. This insight allows us to design practical two-electrode 25 cm^2 Zn dynamic windows, the first examples of RME devices with WISe. We also establish a link between the morphology of the Zn electrodeposits and the optical contrast of the transparent electrodes during switching. Taken together, these studies highlight a potential design strategy for the construction of RME dynamic windows.
 [DOI: 10.1149/1945-7111/ad0494]

Manuscript submitted September 20, 2023; revised manuscript received October 12, 2023. Published November 9, 2023.

Supplementary material for this article is available online

Dynamic windows exhibit electronically controlled transmission and have received much attention for their ability to improve the energy efficiency and aesthetics of buildings.[1–6] Although current methods of designing dynamic windows such as through the use of electrochromic materials or polymer-dispersed liquid crystals (PDLC) are viable, they have limitations that prevent widespread adoption.[7–10] For electrochromic windows, problems associated with color, optical contrast, durability, and cost have prevented widespread adoption.[11–13] Furthermore, PDLC windows are only appropriate in niche applications in which switching to a bright hazy state is tolerable, as opposed to a tinted state that maintains image fidelity.[14,15]

Reversible metal electrodeposition is a promising method of constructing dynamic windows with adjustable tinting.[16,17] RME windows are typically composed of three main components.[18–20] These components are a transparent conducting working electrode such as tin-doped indium oxide (ITO), a counter electrode to charge balance the device, and a gel or liquid electrolyte containing salts of colorless metal ions.[21–23] To darken the window, a reducing potential is applied to the working electrode, which causes the metal ions in the electrolyte to be electrodeposited in their metallic form, thus reducing device transmission.[24–26] The transmission level is controlled through the amount of time the voltage is applied to the window, which dictates the thickness of the metal electrodeposits on the working electrode.[27–29] When an oxidation potential is applied to the darkened working electrode, the metal is stripped off the working electrode and returned to its ionic form, which restores the transparency of the device.[27,30] This process can also be controlled by the amount of time the voltage is applied, allowing the window to achieve a wide range of transmission levels. Due to the opacity of metal films, RME devices can reach privacy-level transmission values (<0.1%) within minutes of tinting.[30–34]

Recently, the reversible electrodeposition of Zn in aqueous electrolytes using Zn salts has emerged as a promising strategy for RME windows due to the high optical contrast and fast switching times of these devices.[35,36] However, the slow accumulation of insoluble products such as $Zn(OH)_2$ and ZnO on the working electrode surface limits long-term device cycling. These undesired side products are inherent to aqueous Zn electrolytes when used in dynamic windows because of the large thermodynamic driving force for water splitting (+0.76 V vs Zn/Zn^{2+}), which facilitates the formation of these side products.[37,38]

In this manuscript, we explore a novel method of constructing dynamic windows through the use of water in salt electrolyte(s) (WISe). WISe are solutions in which the number of salt ions outnumbers the number of water molecules, and therefore the salt ions act as the solvent while the solution remains liquid.[39–41] WISe have been widely used in batteries because of their wider electrochemical windows than salt-in-water electrolytes due to the reduced reactivity of the coordinated water.[42–47] Zn-ion batteries using Zn WISe have been found to produce less dendritic Zn electrodeposits, cycle longer, and produce fewer side reactions than those with traditional electrolytes.[48,49] These properties would be beneficial to WISe dynamic windows if they can be transferred over. Specifically, we hypothesize that the accumulation of irreversible ZnO and $Zn(OH)_2$ side products on transparent working electrodes observed with dynamic windows using aqueous Zn electrolytes can be avoided using Zn WISe due to the decreased reactivity of the coordinated water in WISe. In this manuscript, we design a novel class of WISe dynamic windows based on reversible Zn electrodeposition. We find that the use of WISe in dynamic windows incorporates the advantageous properties of WISe in batteries, and we elucidate links between Zn electrodeposit morphology and window performance. XRD results indicate that electrodeposits produced from the Zn WISe systems consist solely of Zn without significant quantities of ZnO and $Zn(OH)_2$, which is beneficial to device cyclability. However, the morphology the Zn WISe electrodeposits is less compact than those obtained from aqueous Zn electrolytes, which presents a challenge to using Zn WISe systems in dynamic windows in their current form. Regardless, the results from these studies will inform future electrolyte design for practical Zn dynamic windows.

Experimental

Three-electrode cyclic voltammetry (CV) experiments were conducted using separate Zn metal foils (Leishent, 99.9%) as reference and counter electrodes in a 2 cm by 2 cm glass cuvette with 5 ml of electrolyte. Zn is used as a reference electrode as is commonly done in other contexts for reversible Zn electrodeposition.[50,51] Experiments with $K_3Fe(CN)_6$ (Sigma Aldrich, 99.0%) of the Zn reference electrode before and after CVs in the WISe systems show that the Zn reference is stable (Fig. S1). Pt nanoparticles (Sigma Aldrich, 3 nm in diameter) were deposited on ITO on glass (Xinyan Technology, 15 Ω sq^{-1}) by spray coating a 3:1 vol% dispersion of water and Pt. The Pt-modified ITO on glass surfaces were then annealed in air for 20 min at 200 °C. These surfaces served as the working electrodes (3 cm^2 geometric

[z]E-mail: cbarile@unr.edu

surface area). As previously reported, the Pt nanoparticles function as an inert layer that facilitates metal nucleation and improves electrodeposit uniformity.[52,53] Electrochemical measurements were performed using a VSP-300 Biologic potentiostat. All voltammograms presented in this manuscript are the second cycle unless otherwise stated and were performed at a scan rate of 50 mV s^{-1}. All voltammograms presented are iR compensated. For each electrolyte, the solution resistance was obtained using the ZIR function in the EC-lab software provided by Biologic. The ZIR function calculates the solution resistance by measuring the impedance at open circuit potential using a frequency of 100 kHz and a sinus amplitude of 20 mV. The impedances were recorded four times, and the average of these values was used. The uncompensated resistance was thus obtained from the ZIR function and ranged from 7–37 Ω for the WISe systems. The CVs were 100% compensated using these uncompensated resistances with an after-the-scan protocol, which is the method that is most recommended by others.[54] An Ocean Optics FLAME-S-VIS-NIR spectrometer with an Ocean Insight HL2000-FHSA light source was used for transmission measurements. The spectrometer uses a two-point calibration with dark (0% transmission) and light (100% transmission) points. The electrolyte in the cuvette without the Pt-modified ITO electrode served as the standard for 100% transmission for all optical measurements. The various electrolyte compositions are listed in the figure captions. $Zn(CH_3COO)_2$ (99%) and KCH_3COO (99%) were obtained from Oakwood Chemicals. $ZnCl_2$ (98%) was purchased from Fisher Scientific, and polyethylene glycol (1500 average molecular weight) was procured from Sigma Aldrich.

To construct two-electrode 25 cm^2 dynamic windows, Cu tape with conductive adhesive was first placed on the perimeter of the Pt-modified ITO on glass for electrical connection. Zn mesh with a wire diameter of 3 mm and an interwire spacing of about 1 cm was used as the counter electrode. The mesh was sandwiched between a nonconductive piece of glass and the Pt-modified ITO on glass working electrode. In future studies, we will construct Zn meshes with thinner metal grid lines to increase transparency. Although the design of thin metal grid lines is beyond the scope of this manuscript, transparent metal meshes have been developed for other systems.[55] Butyl rubber (Solargain, Quanex, Inc.) around the device edges allowed for sealing of the devices with a spacing of about 5 mm. Electrolyte was then syringed into the device stack through the sealant. For 25 cm^2 two-electrode devices, a value of 100% transmission was defined as open air. Transmission data were collected through an opening in the Zn grid at the device center. A small fraction of the light from the light source was blocked by the grid wires, which causes the starting transmission values of the two-electrode devices to be less than those measured in three-electrode cells. The Zn grids are only used in the two-electrode devices.

A JOEL JSM-6010LA microscope operating at a voltage of 20 kV was used to collect scanning electron microscope (SEM) images. X-ray diffraction (XRD) experiments were carried out with a Bruker D8 X-ray Diffractometer.

Results and Discussion

To study the potential benefits of using a WISe in a dynamic window, we first focus our study on a relatively simple Zn-based WISe that only contains $ZnCl_2$ and H_2O. The evaluation of this Zn-based WISe began with the study of how the $ZnCl_2$ concentration in the WISe affects electrolyte spectroelectrochemistry (Fig. 1). Due to large concentration of salts in WISe, we report electrolyte concentrations in molality (m) as is common practice[40,41] rather than molarity (M). The electrodes using 8 m, 15 m, 20 m, and 30 m WISe all exhibit similar optical performance, giving an optical contrast (defined as the difference between maximum and minimum transmission at 600 nm measured during the CV cycle) of about 10% (Fig. 1B, black, red, and blue lines). The differences in starting transmissions in Fig. 1B occur because the data were taken from the second CV cycles, and so any irreversibility from the first cycle resulted in a decreased starting electrode transmission. The second cycle was chosen for most of the analysis in this manuscript because the first cycle analysis is complicated by initial nucleation of Zn electrodeposits. As such, the second cycle is the most representative of electrolyte performance.[39] The CVs, however, of the 8 m, 15 m, 20 m, and 30 m $ZnCl_2$ significantly differ (Fig. 1A). The CV of 8 m $ZnCl_2$ contains the highest magnitude of current density, both for Zn deposition and stripping (Fig. 1A, black line). Increasing the concentration of $ZnCl_2$ decreases the magnitude of the current densities for both processes (Fig. 1A, red, blue, and green lines). This trend is opposite to the typical behavior of normal salt-in-water electrolytes in which increasing metal ion concentration results in increased current density because more metal ions are available to be plated.[39] Previous battery literature using $ZnCl_2$ WISe shows that increasing the WISe concentration increases the overpotential of Zn electrodeposition, which indicates that Zn electrodeposition is impeded at higher $ZnCl_2$ concentrations. In WISe, $ZnCl_2$ serves as the solvent, and increasing the $ZnCl_2$ concentration increases the strength of the ionic network, making it more difficult for Zn ions to dissociate and deposit. This rationalization explains why the magnitudes of the current densities for the $ZnCl_2$ WISe are lower at higher $ZnCl_2$ concentrations. We also interpret these results in the context of the activity of Zn^{2+}, which is defined as the product of Zn^{2+} concentration and the Zn^{2+} activity coefficient. Zn^{2+} activity is reported to increase with $ZnCl_2$ concentration in WISe systems because of both the increased Zn^{2+} concentration and an increase in the Zn^{2+} activity coefficient due to changes in the Zn^{2+} hydration structure.[42,45] Because the higher concentration WISe exhibit lower current densities in our CVs, Zn^{2+} activity alone cannot explain the differences in electrochemistry observed. However, it is known in WISe electrolytes that at high salt concentrations, complex ion networks form,[56] which affect other electrolyte parameters such as mass transfer rates that in turn can affect electrolyte spectroelectrochemistry.

In all cases, the onset potential for Zn electrodeposition is more positive than −150 mV vs Zn/Zn^{2+}, indicating that there is a low overpotential for metal electrodeposition on the ITO electrodes. Furthermore, we note that the concentration of Zn^{2+} does not change significantly during the course of the CV experiments. For example, for the 8 m $ZnCl_2$ WISe, which exhibits the highest amount of charge passed during deposition, only about 0.01% of the Zn^{2+} ions in the electrolyte are electrodeposited onto the ITO.

Compared to previous work on $ZnCl_2$-based salt-in-water electrolytes, the $ZnCl_2$ WISe exhibit much poorer optical contrast, while attaining a similar or larger magnitude of current density during the CV.[1,2] This difference in optical response is the result of differences in Zn electrodeposit morphology between the salt-in-water and WISe systems. The lower optical contrasts resulting from the WISe-based films is explained by nonuniform Zn electrodeposits that are inefficient at blocking light on the microscale (*vide infra*). Furthermore, the electrodes used in the various electrolytes possess similar optical contrasts despite the large differences in the associated CVs. These results indicate that a change in electrodeposition current density, and therefore a change in the quantity of Zn electrodeposited does not affect the ability of the films to block light. Due to this poor electrodeposit morphology, we next investigate the use of polymer additives in WISe to improve optical contrast.

We select 1500 molecular weight polyethylene glycol (PEG) as the polymer additive as previous studies have shown it to be effective in improving cyclability and optical contrast by increasing the compactness and uniformity of the Zn electrodeposits on the microscale. Previously studied Zn salt-in-water electrolytes show that the addition of PEG promotes the growth of the (002) crystal face of Zn through a surface-adsorption mechanism.[39] The predominance of the (002) face is linked to enhanced cycle life in Zn batteries due to the prismatic-like structure of the electrodeposits.[57,58] We also select to use a concentration of 15 m $ZnCl_2$ for the PEG studies because this electrolyte possesses the

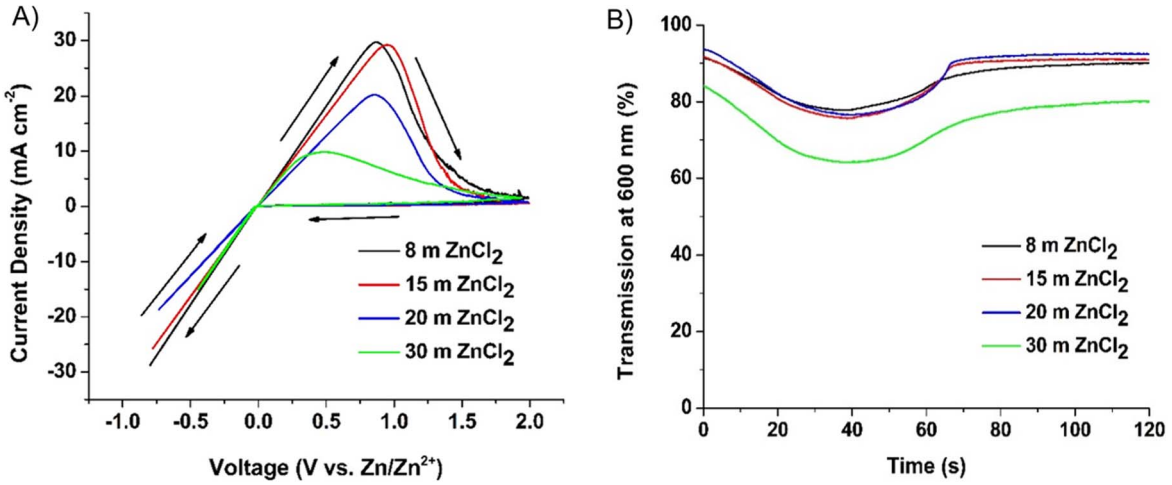

Figure 1 Cyclic voltammograms (A) and corresponding transmission at 600 nm (B) of Pt-modified ITO electrodes using 8 m $ZnCl_2$ (black line), 15 m $ZnCl_2$ (red line), 20 m $ZnCl_2$ (blue line), or 30 m $ZnCl_2$ (green line).

highest Coulombic efficiency (96.3%) among the various concentrations.

In Fig. 2, we evaluate the effect of PEG concentration on the 15 m $ZnCl_2$ WISe. Increasing the concentration of PEG in the electrolyte decreases the magnitudes of both deposition and stripping current densities in the CVs (Fig. 2A). This result is expected because the polymer acts as an inhibitor of metal electrodeposition as has been observed previously in other polymer-modified RME systems.[20,39] The electrode in the 0.1 wt% PEG electrolyte exhibits a reversible optical contrast of ∼30% (Fig. 2B, black line), which is significantly higher than the ∼15% optical contrast obtained in the absence of PEG (Fig. 1B, red line). Increasing the PEG content to 1 wt% further improves the optical contrast to ∼35% (Fig. 2B, red line). This improvement in optical contrast along with the decreased current density in the CV indicates that the PEG increases optical contrast not by increasing the Zn deposition rate, but by altering the morphology of the Zn electrodeposits such that they more effectively block light. Further increasing the concentration of PEG to 5 wt% dramatically decreases the current density in the CV, and the optical contrast is worse than the 0.1 and 1 wt% cases. These results indicate that Zn electrodeposition in the 5 wt% electrolyte is too strongly inhibited so that the improved electrodeposit morphology does not compensate for the reduction in Zn electrodeposition kinetics. Despite the modest improvements imparted by the addition of PEG, the optical contrasts attained are not comparable to those of corresponding Zn salt-in-water electrolytes.[1,2,36,39] Similarly to the $ZnCl_2$ WISe without PEG, the electrodes used with $ZnCl_2$ WISe with PEG possess similar optical contrast to each other despite large differences in current densities. This observation provides further evidence that the inherent morphology of the $ZnCl_2$ WISe is not only poor at blocking light, but difficult to manipulate using polymer additives. As such, we continued our investigation of Zn WISe using other electrolyte chemistries.

KCH_3COO-$Zn(CH_3COO)_2$ systems that exhibit good reversibilities have previously been used in Zn-ion batteries.[59–61] A CV of 30 m KCH_3COO and 1 m $Zn(CH_3COO)_2$ (30K1Zn) using a Pt-modified ITO electrode with a voltage range of −1 V to 1 V possesses a Zn electrodeposition peak at around −0.5 V, which is followed by a further increase in cathodic current (Fig. 3A, red line). Note that the voltage ranges described are those applied by the potentiostat and are *iR* uncompensated, while the CVs in Fig. 3 and all others in this manuscript are *iR* compensated, which results in shifting of the voltage scan ranges. The corresponding transmission of the electrode exhibits poor optical reversibility (Fig. 3B, red line). After three CV cycles from −1 V to 1 V, the electrode possesses negligible current density (Fig. 3A, blue line). Taken together, these results indicate that ITO degradation occurs at potentials more negative than the Zn deposition peak. Specifically, the In_2O_3 and SnO_2 are reduced to elemental In and Sn.[62] In contrast, narrowing the scan range to −0.6 V to 1 V produces a CV that avoids the ITO degradation region (Fig. 3A, black line). The electrode transmission during this CV therefore possesses greater optical contrast and

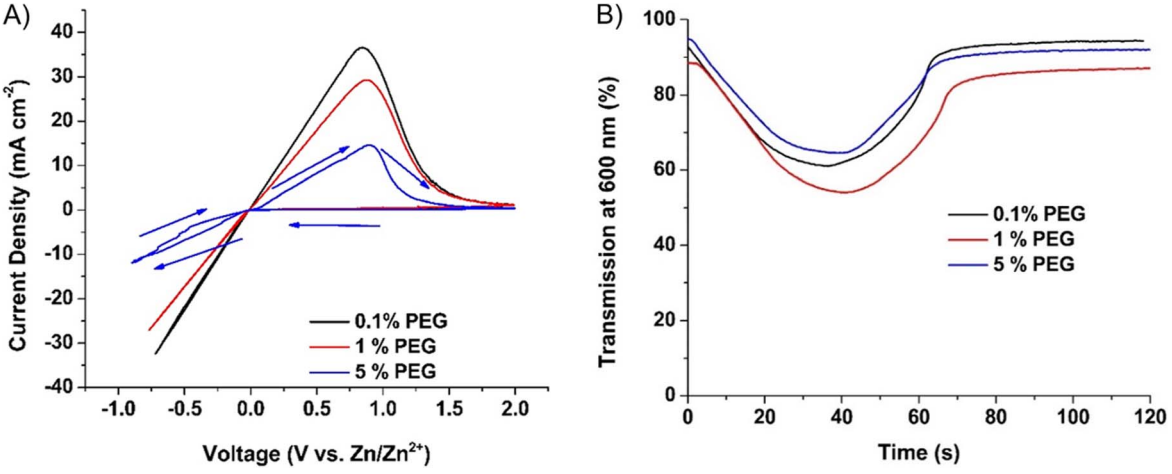

Figure 2. Cyclic voltammograms (A) and corresponding transmission at 600 nm (B) of Pt-modified ITO electrodes using 15 m $ZnCl_2$ with 0.1 wt% PEG (black line), 1 wt% PEG (red line), or 5 wt% PEG (blue line).

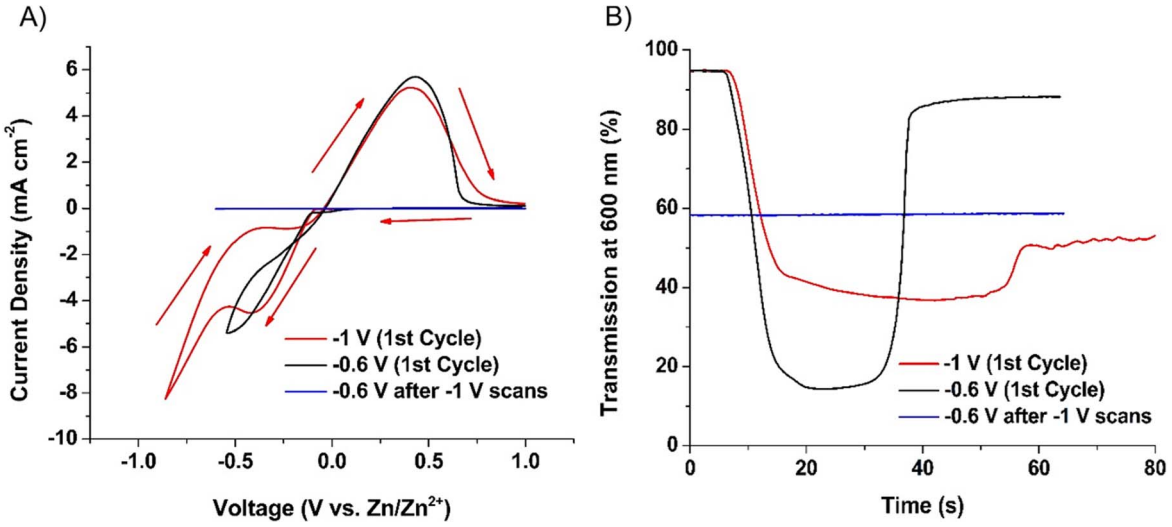

Figure 3. Cyclic voltammograms (A) and corresponding transmission at 600 nm (B) of Pt-modified ITO electrodes using 30 m KCH_3COO and 1 m $Zn(CH_3COO)_2$ (30K1Zn). The black and red lines are first cycle CVs, while the blue line is a cycle obtained after three CVs were conducted with a −1 V cathodic limit. While the voltage limits listed are those applied by the potentiostat and are *iR* uncompensated, the CVs presented, along with all others in the manuscript are *iR* compensated.

reversibility (Fig. 3B, black line). For these reasons, we selected an *iR* uncompensated voltage range of −0.6 V to 1 V (presented CVs are *iR* compensated) for additional testing of the KCH_3COO-$Zn(CH_3COO)_2$ WISe.

To assess the role of acetate in the KCH_3COO-$Zn(CH_3COO)_2$ WISe, we varied the concentration of KCH_3COO in the electrolyte. The 30K1Zn solution produces a CV with a maximum current density magnitude of about 5 mA cm^{-2} during both Zn deposition and stripping (Fig. 4A, black line). Switching the electrode in the 30K1Zn solution gives rise to a nearly reversible transmission change with an optical contrast of about 80% (Fig. 4B, black line). This electrode displays similar behavior across all visible wavelengths during deposition (Fig. S2). In this manuscript, we choose 600 nm as a representative value to aid in comparison with previous Zn electrodeposition works.[1,38] Decreasing the KCH_3COO concentration from 30 m to 20 m results in reduced current density for both Zn electrodeposition and stripping (Fig. 4A, red line). The corresponding electrode transmission using the 20K1Zn electrolyte possesses a much smaller optical contrast (Fig. 4B, red line). These results indicate that an increase in KCH_3COO increases Zn electrodeposition kinetics and improves Zn electrodeposit morphology. Attempts to further increase the KCH_3COO concentration beyond 30 m resulted in insoluble solutions. Interestingly, decreasing the KCH_3COO concentration to 10 m results in a CV that possesses much greater current density magnitudes than either 20K1Zn or 30K1Zn (Fig. 4A, blue line). The lower concentration of KCH_3COO at 10 m renders the effective volumetric (molar) concentration of Zn^{2+} highest in the 10K1Zn electrolyte. This observation follows the results and discussion of Fig. 1 in which lower concentrations of the $ZnCl_2$ WISe exhibit greater magnitudes of current density. However, the larger magnitude of current density in the 10K1Zn CV does not translate to a larger optical contrast than 30K1Zn, which has a lower amount of current density. Further examination of the difference in optical performance of the electrolytes shows similar levels of reversibility between the electrodes despite large differences in current density. The reason why the trend of current density increasing with decreasing total concentration breaks when going from 30K1Zn to 20K1Zn is unclear, but it suggests that intermolecular forces and dynamics that govern Zn^{2+} activity are multifaceted and heavily depend upon the relative concentrations of H_2O, KCH_3COO, and $Zn(CH_3COO)_2$. These factors may also influence the morphology of the electrodeposits as the electrode used in 20K1Zn WISe possesses a lower optical contrast than both the higher and lower concentration 30K1Zn and 10K1Zn. Nevertheless,

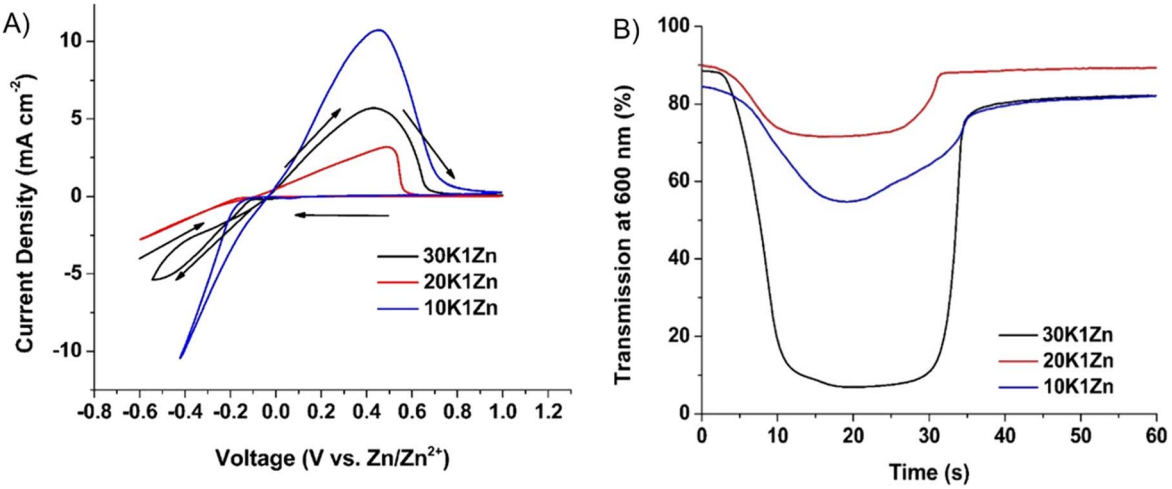

Figure 4. Cyclic voltammograms (A) and corresponding transmission at 600 nm (B) of Pt-modified ITO electrodes using 1 m $Zn(CH_3COO)_2$ and various concentrations of KCH_3COO: 10 m (10K1Zn, blue line), 20 m (20K1Zn, red line), or 30 m (30k1Zn, black line).

we select the 30K1Zn electrolyte for the remainder of our studies with this WISe system due to its superior optical contrast.

As the 30K1Zn is composed of multiple components, we investigated the individual electrolyte components to evaluate potential synergies in the full electrolyte. The CV of the 30 m KCH_3COO electrolyte without Zn^{2+} ions shows low current density (Fig. 5A, blue line). Based on previous literature and also the results described in Fig. 3, the cathodic current observed in this CV is attributed to ITO degradation to elemental In and Sn, and the anodic current is due to the subsequent stripping of these metals. This interpretation is supported by the completely irreversible transmission change of the electrode (Fig. 5B, blue line).

An electrolyte that contains only 1 m $Zn(CH_3COO)_2$, when compared to the full 30K1Zn WISe, possesses similar deposition current density and a significantly lower maximum oxidation current (Fig. 5A, red and black lines). This finding suggest that a similar amount of Zn metal is electrodeposited from the salt-in-water electrolyte as in the water-in-salt electrolyte, but that the particles formed from the salt-in-water electrolyte are harder to strip. The salt-in-water electrolyte possesses an optical contrast of ∼20% compared to the ∼80% when 30 m KCH_3COO is included to form the water-in-salt electrolyte (Fig. 5B, red and black lines). These results suggest that the KCH_3COO improves the morphology of the Zn electrodeposited layer, allowing it to more efficiently block light and facilitate metal stripping. Previous studies demonstrate that aqueous $Zn(CH_3COO)_2$ electrolytes result in significant quantities of ZnO and $Zn(OH)_2$ in the Zn electrodeposits, which adversely affect metal deposition and stripping processes.[35] Water in the aqueous electrolytes facilitates the formation of these side products. The addition of large quantities of KCH_3COO enables WISe formation,[59–61] which suppresses water reactivity and therefore the formation of ZnO and $Zn(OH)_2$. Taking together, the results of Fig. 5 indicate that there is synergy between the components of the 30K1Zn electrolyte that allow it to function with high optical contrast and good reversibility.

We next compare the Coulombic efficiency (CE) of the various WISe (Fig. 6). CE is defined as the amount of charge passed during Zn stripping divided by the amount of charge passed during Zn electrodeposition and is used to evaluate the electrochemical reversibility of the metal electrodeposition process. The $ZnCl_2$ only WISe shows a trend across the 15 m, 20 m, and 30 m $ZnCl_2$ in which an increase in concentration decreases electrolyte CE. These results are expected based on the discussion surrounding Fig. 1 in which a similar trend can be seen in the optical reversibilities of the electrodes and the current density magnitudes of the CVs. However, the 8 m $ZnCl_2$ WISe does not follow this trend as it has lower CE than 15 m or 20 m $ZnCl_2$, but this exception is also seen in the spectroelectrochemical data (Fig. 1, black line).

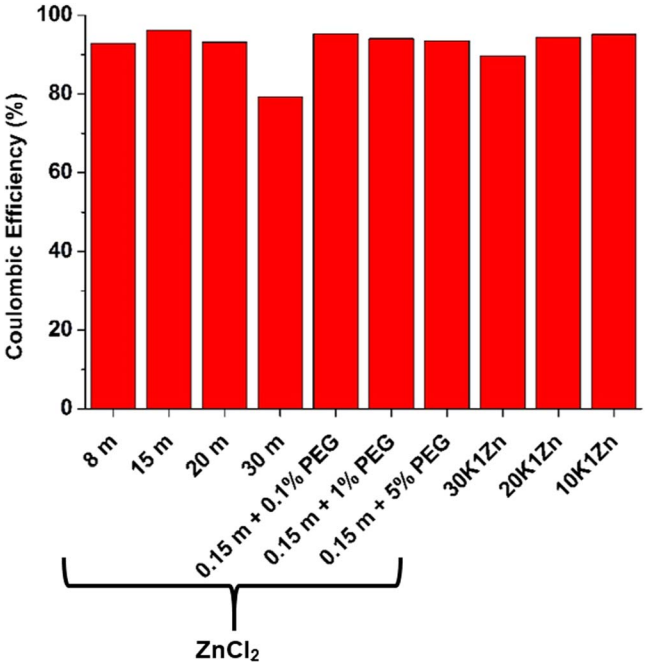

Figure 6. Coulombic efficiencies of the CVs electrolytes with various compositions.

Similarly, the CEs of the $ZnCl_2$ with PEG WISe also exhibit a trend that follows the corresponding spectroelectrochemical data (Fig. 2). An increase in the concentration of PEG decreases the CEs of the electrolytes because the polymer is a metal electrodeposition inhibitor. The similar CE between 15 m $ZnCl_2$ and 15 m $ZnCl_2$ with 0.1% PEG along with the higher optical contrast of the electrode used with 15 m $ZnCl_2$ with 0.1% PEG (Fig. 2, black line compared to Fig. 1, red line) inform our decision to use 15 m $ZnCl_2$ with 0.1% PEG during subsequent long-term cycling experiments.

The CEs of the KCH_3COO-$Zn(CH_3COO)_2$ WISe show a clear trend in which lower concentrations of KCH_3COO gives rise to higher CEs in a manner similar to the CEs of the $ZnCl_2$ WISe. However, due to the superior optical contrast of the electrode used with the 30K1Zn electrolyte (Fig. 4B, we selected the 30K1Zn electrolyte for subsequent long-term cycling experiments.

Before discussing the cycling results, we directly compare the spectroelectrochemical properties of two representative electrolytes from each WISe system. The CVs and transmission profiles for the

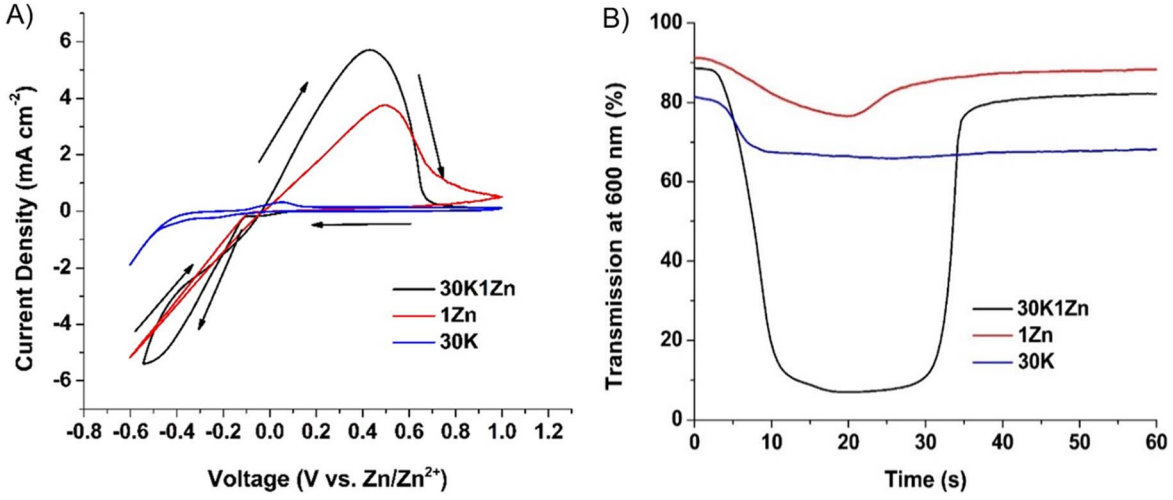

Figure 5. Cyclic voltammograms (A) and corresponding transmission at 600 nm (B) of Pt-modified ITO electrodes using 1 m $Zn(CH_3COO)_2$ (1Zn, red line), 30 m KCH_3COO (30 K, blue line), and 1 m $Zn(CH_3COO)_2$ and 30 m KCH_3COO (30K1Zn, black line).

30K1Zn and 15 m $ZnCl_2$ with 0.1% PEG are dramatically different. In particular, the CV of the 15 m $ZnCl_2$ system possesses a much larger magnitude of current density than the 30K1Zn electrolyte both during the cathodic and anodic processes (Fig. 7A). These differences in current density as well as the CEs of the electrolytes indicate that much more Zn electrodeposition and stripping occurs from the 15 m $ZnCl_2$ electrolyte. This finding is in line with the Zn^{2+} volumetric concentrations (molarity) of the two electrolytes. Specifically, the Zn^{2+} molarity of the 15 m $ZnCl_2$ electrolyte is significantly higher (8.8 M) than that of 30K1Zn (0.4 M). Despite the lower concentration of Zn^{2+} in 30K1Zn and the resulting lower current density, the electrode using the 30K1Zn exhibits a much higher optical contrast (Fig. 7B). This result demonstrates that on a per charge basis, the Zn electrodeposits produced from the 30K1Zn are much more effective at blocking light, which suggests that they possess a more uniform morphology. However, both categories of WISe show similarly high levels of reversibility and have comparable reversibility to salt-in-water Zn electrolytes, despite both electrolytes having a lower CE than what is reported for salt-in-water Zn electrolytes.[1,38] These results combined with XRD data (*vide infra*) showing that Zn WISe produce Zn electrodeposits without any ZnO or $Zn(OH)_2$ side products suggest that morphology is the determining factor for optical performance.

This conclusion led us to explore the surface morphology of Zn electrodeposits formed by the different electrolytes through SEM (Fig. 8). The images of the electrodeposits produced from 15 m $ZnCl_2$ show that the electrode consists of large, nonuniform Zn particles (Figs. 8A and 8B). There are also gaps between the deposited particles, which indicates that the layer is inefficient at blocking light. Furthermore, the irregular particle sizes are expected to create issues in long-term cycling as they are difficult to strip.[63,64] Larger, irregularly-shaped particles have fewer points of contact with the electrode, which impedes the kinetics of stripping as charge cannot flow as easily between the electrodeposits and the underlying ITO electrode. In contrast, the electrodeposits produced from the 30K1Zn WISe consist of long fibrous-like structures that connect to each other to form a flat and more even layer (Figs. 8C and 8D), which gives rise to the greater optical contrast of the electrode using 30K1Zn. At higher magnification, it is revealed that these long structures are comprised of smaller particles that layer together. The interconnected nature of the electrodeposits is expected to allow for better stripping as there are more points of contact with the electrode. As such, a window containing 30K1Zn solution should exhibit better long-term cycling than a window containing the 15 m $ZnCl_2$ electrolyte. The differences in electrodeposit morphology between the two electrolytes can be further explained by differences in nucleation and growth dynamics. By comparing the chronoamperometry data to idealized instantaneous and progressive growth models, the predominant nucleation-growth mechanism can be revealed.[65] In the instantaneous model, nucleation only occurs during the initial stages of electrodeposition and is followed by growth. In the progressive model, nucleation occurs continuously throughout electrodeposition together with growth. The modeling results indicate that the 30K1Zn electrolyte largely follows the instantaneous model, while the 15 m $ZnCl_2$ electrolyte exhibits a mixture of instantaneous and progressive models (Fig. S3). The more progressive nature of the electrodeposits produced in the 15 m $ZnCl_2$ electrolyte helps to explain why the Zn electrodeposits in this case are much more nonuniform than those generated from the 30K1Zn electrolyte.

XRD of Zn electrodeposits generated from the 15 m $ZnCl_2$ solution possess three intense peaks at 35°, 38°, and 42°, which are ascribed to the (002), (100), and (101) Zn crystal faces (Fig. 9, black line). The spectrum also shows minor peaks at 53°, 70°, and 78°, which are due to (103), (110), and (004) crystal faces.[66–69] Due to the large quantity of Zn electrodeposits produced from the 15 m $ZnCl_2$ electrolyte that supports high current density, underlying ITO peaks are not observed. Moreover, the Zn peaks in the spectrum are present in similar intensity ratios as those seen in Zn electrodeposits produced in batteries using $ZnCl_2$ WISe,[59] indicating that the electrodeposits are comprised of metallic Zn without significant crystalline ZnO or $Zn(OH)_2$ side products. This result indicates that any degradation in device cycling observed would be attributed to the morphology of the window rather than the formation of ZnO or $Zn(OH)_2$.

The XRD spectrum of the Zn electrodeposits formed from the 30K1Zn display both Zn and ITO diffraction peaks (Fig. 9, red line) because a smaller quantity of Zn was plated during deposition due to the lower current density of this electrolyte. The ITO peaks are assigned using a control experiment measuring the spectrum of a Pt-modified ITO working electrode without Zn electrodeposits (Fig. 9, blue line). Aside from the ITO peaks, there are two peaks which can be ascribed to Zn faces- a low-intensity peak at 42° due to Zn(101) and a high-intensity peak at 38° due to Zn(002). The predominance of the (002) crystal plane, a flat hexagonal face, gives rise to the relative smoothness seen in the SEM for the Zn electrodeposits formed from 30K1Zn.[70]

The morphology of the Zn electrodeposits has ramifications for two-electrode device cycleability. In particular, a window with 30K1Zn cycles at a greater optical contrast and endures many more cycles than a window containing 15 m $ZnCl_2$ with 0.1% PEG (Fig. 10). Each window was cycled until the contrast ratio, which is defined as the difference between the maximum and minimum transmission during a cycle, reached 20%. As mentioned above, the

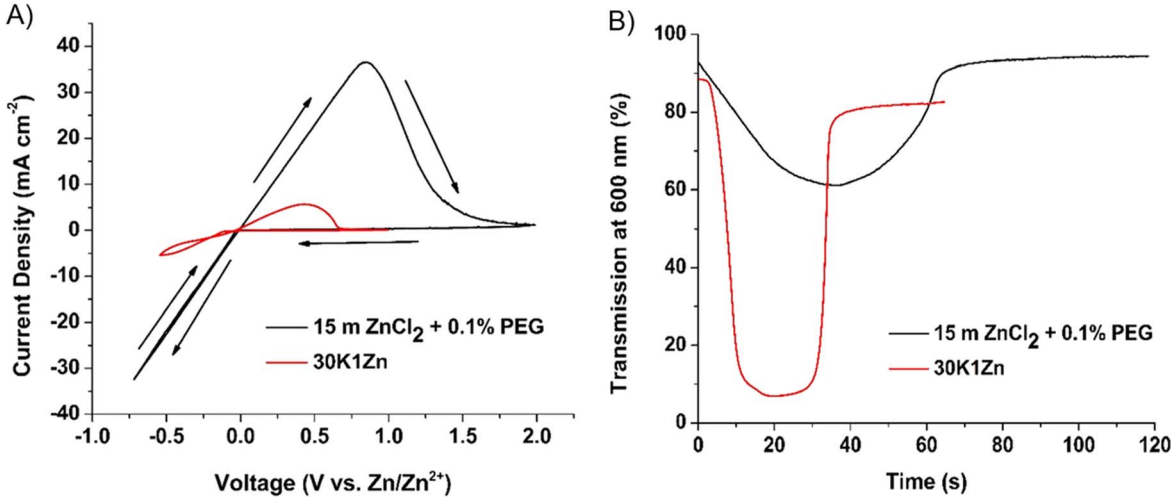

Figure 7. Cyclic voltammograms (A) and corresponding transmission at 600 nm (B) of Pt-modified ITO electrodes using 15 m $ZnCl_2$ and 0.1 wt% PEG (black line) and 1 m $Zn(CH_3COO)_2$ and 30 m KCH_3COO (30K1Zn, red line).

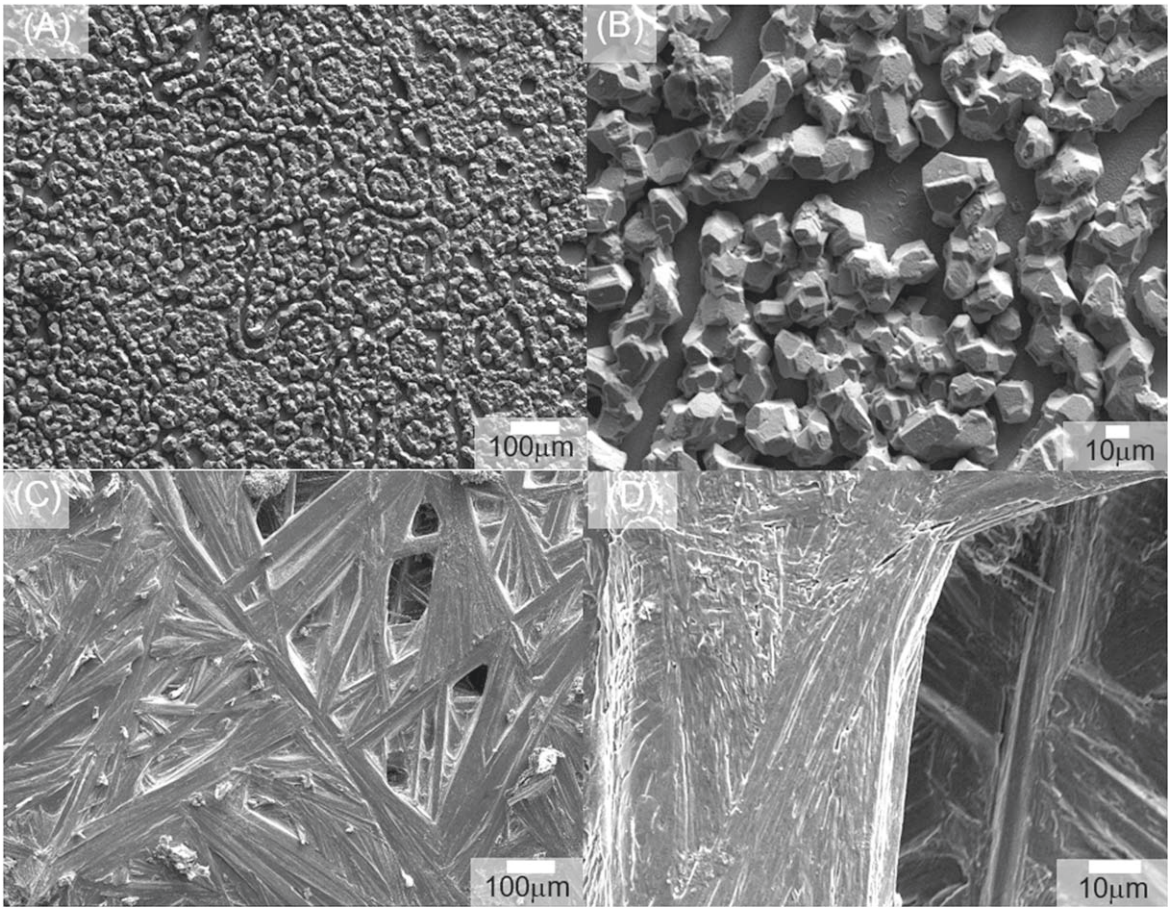

Figure 8. Scanning electron microscopy images of Zn electrodeposits on Pt-modified ITO electrodes with a transmission at 600 nm of 30%. Images in panels A and B were obtained on electrodes produced using chronoamperometry at −0.6 V in the 15 m $ZnCl_2$ electrolyte, while the images in panels C and D were obtained on electrodes produced using chronoamperometry at −0.3 V in the electrolyte containing 30 m KCH_3COO and 1 m $Zn(CH_3COO)_2$.

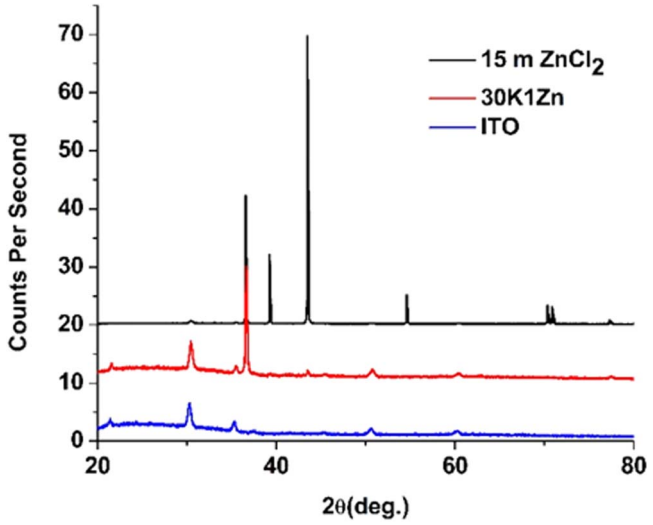

Figure 9. X-ray diffraction spectra of Pt-modified ITO working electrodes with Zn electrodeposits produced from electrolytes containing 15 m $ZnCl_2$ (black line) or 30 m KCH_3COO and 1 m $Zn(CH_3COO)_2$ (red line). XRD was performed on the electrodes using at −0.6 V in the 15 m $ZnCl_2$ electrolyte or at −0.3 V in the electrolyte containing 30 m KCH_3COO and 1 m $Zn(CH_3COO)_2$ until the electrode reached 30% transmission. The spectra displayed in blue is obtained using a Pt-modified ITO working electrode control and shows peaks that are ascribed to ITO.

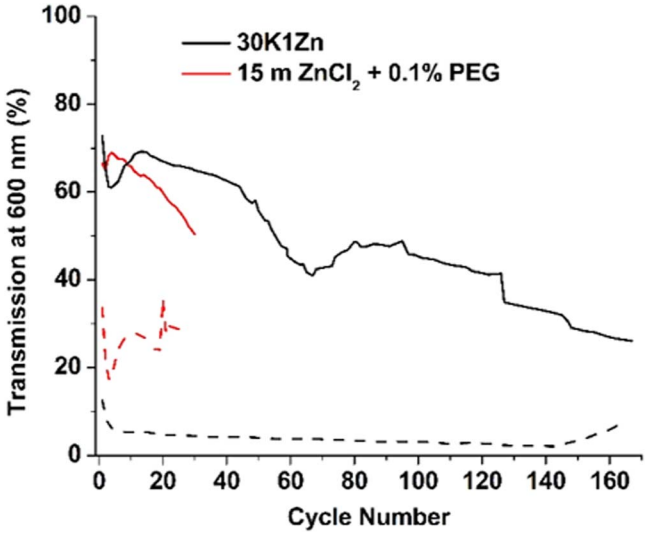

Figure 10. Maximum (solid lines) and minimum (dashed lines) transmission values at 600 nm of 25 cm^2 Zn dynamic windows. For the red lines, the window contained a 15 m $ZnCl_2$ electrolyte with 0.1 wt% PEG, and each switching cycle utilized −0.6 V for 90 s to induce metal electrodeposition and +1 V for 90 s to elicit metal stripping (Fig. S4A). For the black lines, the window contained a 30 m KCH_3COO and 1 m $Zn(CH_3COO)_2$ electrolyte, and each switching cycle utilized −0.3 V for 30 s to induce metal electrodeposition and +0.3 V for 30 s to elicit metal stripping (Fig. S4B).

Zn(002) facet favored in the 30K1Zn electrolyte allows for a

smoother morphology, which is beneficial for optical contrast, stripping kinetics, and cycleability. Interestingly, the window with the 30K1Zn electrolyte displays enhanced cycleability despite the lower Coulombic efficiency of the 30K1Zn electrolyte (90%) compared to 15 m $ZnCl_2$ with 0.1% PEG (96%). This finding suggests that differences in the morphological evolution during cycling play a role in determining cycle life. Regardless, the cycle lives of both of the WISe windows presented here are insufficient for practical applications. In future work, we will seek to more fully understand degradation mechanisms so that more robust WISe devices can be constructed.

Conclusions

In this manuscript, we examine the use of WISe as electrolytes in Zn-based RME dynamic windows. We systematically study two families of WISe by examining the effects that concentration, composition, polymer additives, and different voltage profiles have on spectroelectrochemical properties including Coulombic efficiency, surface morphology, and optical contrast and reversibility. We describe a relationship between Zn electrodeposit morphology and the optical reversibility of Zn electrodeposition and stripping. Using the best-performing electrolyte, we successfully constructed two-electrode 25 cm^2 dynamic windows that cycle about 100 cycles with 50% optical contrast. This work serves as a foundation for future studies with dynamic windows with WISe.

Acknowledgments

This material is based upon work supported by the National Science Foundation under Grant No. ECCS2127308. We gratefully acknowledged the support of National Science Foundation (CHE-1429768) for purchasing the X-ray diffractometer. SEM-EDX analysis was performed in the Mackay Microbeam Laboratory at UNR, and we thank J. Desormeau for his kind assistance.

ORCID

Christopher J. Barile https://orcid.org/0000-0002-4893-9506

References

1. D. C. Madu, S. M. Islam, H. Pan, and C. J. Barile, *J. Mater. Chem. C*, **9**, 6297 (2021).
2. N. L. Sbar, L. Podbelski, H. M. Yang, and B. Pease, *Int. J. Sustain. Built Environ.*, **1**, 125 (2012).
3. M. Aburas, H. Ebendorff-Heidepriem, L. Lei, M. Li, J. Zhao, T. Williamson, Y. Wu, and V. Soebarto, *Energy Build.*, **235**, 110717 (2021).
4. S. L. Eleanor, Y. Mehry, and E. S. Stephen, *Lawrence Berkeley National Laboratory.*, **LBNL**, 54966 (2004).
5. Y. Cui, Y. Ke, C. Liu, Z. Chen, N. Wang, L. Zhang, Y. Zhou, S. Wang, Y. Gao, and Y. Long, *Joule.*, **2**, 1707 (2018).
6. D. Coates, *J. Mater. Chem.*, **5**, 2063 (1995).
7. J. P. Ziegler and B. M. Howard, *Sol. Energy Mater. Sol. C.*, **39**, 317 (1995).
8. J. P. Ziegler, *Sol. Energy Mater. Sol. C.*, **56**, 477 (1999).
9. J. W. Doane, A. Golemme, J. L. West, J. B. Whitehead, and B. G. Wu, *Mol. Cryst. Liq. Cryst. Inc. Nonlinear Opt.*, **165**, 511 (1988).
10. W. Zhang, H. Li, W. W. Yu, and A. Y. Elezzabi, *Small Science*, **1**, 2100040 (2021).
11. S. M. Islam, T. S. Hernandez, M. D. McGehee, and C. J. Barile, *Nat. Energy*, **4**, 223 (2019).
12. G. K. A. Alcaraz, J. S. Juarez-Rolon, N. A. Burpee, and C. J. Barile, *J. Mat. Chem. C*, **6**, 2132 (2018).
13. S. M. Cho et al., *Sol. Energy Mater. Sol. C.*, **179**, 161 (2018).
14. D. Cupelli, F. P. Nicoletta, S. Manfredi, M. Vivacqua, P. Formoso, G. De Filpo, and G. Chidichimo, *Sol. Energy Mater. Sol. C.*, **93**, 2008 (2009).
15. H. Shin, J. W. Ryu, J. S. Gwag, H. M. Lee, J. Y. Hong, S. W. Kim, Y. S. Lee, and J. M. Kim, *J. Korean Phys. Soc.*, **80**, 273 (2022).
16. J. Y. Li and C. J. Barile, *J. Electrochem. Soc.*, **168**, 092501 (2021).
17. G. R. McAndrews, A. L. Yeang, Y. Cai, C. J. Barile, and M. D. McGehee, *Adv. Energy Mater.*, **13**, 2202843 (2023).
18. J. Y. Li, J. S. Juarez-Rolon, S. M. Islam, and C. J. Barile, *J. Electrochem. Soc.*, **166**, D496 (2019).
19. L. S. Arvisu, A. A. Palma, S. M. Islam, and C. J. Barile, *J. Electrochem. Soc.*, **169**, 072502 (2022).
20. M. T. Strand, T. S. Hernandez, M. G. Danner, A. L. Yeang, N. Jarvey, C. J. Barile, and M. D. McGehee, *Nat. Energy*, **6**, 546 (2021).
21. D. D. Miller, J. Y. Li, S. M. Islam, J. F. Jeanetta, and C. J. Barile, *J. Mater. Chem. C*, **8**, 1826 (2020).
22. S. M. Islam and C. J. Barile, *ACS Appl. Mater. Interfaces*, **11**, 40043 (2019).
23. S. M. Islam, A. A. Palma, R. P. Gautam, and C. J. Barile, *ACS Appl. Mater. Interfaces*, **12**, 44874 (2020).
24. T. S. Hernandez, C. J. Barile, M. T. Strand, T. E. Dayrit, D. J. Slotcavage, and M. D. McGehee, *ACS Energy Lett.*, **3**, 104 (2018).
25. T. S. Hernandez, M. Alshurafa, M. T. Strand, A. L. Yeang, M. G. Danner, C. J. Barile, and M. D. McGehee, *Joule.*, **4**, 1501 (2020).
26. S. Islam, C. Fini, and C. Barile, *J. Electrochem. Soc.*, **166**, D333 (2019).
27. S. Araki, K. Nakamura, K. Kobayashi, A. Tsuboi, and N. Kobayashi, *Adv. Mater.*, **24**, OP122 (2012).
28. K. Kanazawa, K. Nakamura, and N. Kobayashi, *Chem. Asian J.*, **7**, 2551 (2012).
29. C. L. DeFoor, J. F. Jeanetta, and C. J. Barile, *ACS Appl. Electron. Mater.*, **2**, 290 (2020).
30. Tsuboi, K. Nakamura, and N. Kobayashi, *Adv. Mater.*, **25**, 3197 (2013).
31. X. Tao, D. Liu, J. Yu, and H. Cheng, *Adv. Opt. Mater.*, **9**, 2001847 (2021).
32. N. N. Greenword and A. Earnshaw, *Chemistry of the Elements* (Butterworth-Heinemann, Oxford, U.K.) 2nd ed. (1997).
33. C. Park, S. Seo, H. Shin, B. D. Sarwade, J. Na, and E. Kim, *Chem. Sci.*, **6**, 596 (2015).
34. S. Bao, K. Tajima, Y. Yamada, M. Okada, and K. Yoshimura, *Appl. Phys. A*, **87**, 621 (2007).
35. S. M. Islam and C. J. Barile, *Adv. Energy Mater.*, **11**, 2100417 (2021).
36. H. I. Kim, E. J. Kim, S. J. Kim, and H. C. Shin, *J. Appl. Electrochem.*, **45**, 335 (2015).
37. P. Vanýsek, *CRC Handbook of Chemistry and Physics* (CRC Press, Boca Raton, Florida) (2002).
38. D. C. Madu, M. V. Lilo, A. A. Thompson, H. Pan, M. D. McGehee, and C. J. Barile, *ACS Appl. Mater. Interfaces*, **14**, 47810 (2022).
39. X. Ji, *eScience*, **1**, 99 (2021).
40. S. B. Pillai, R. J. Wilcox, B. G. Hillis, B. P. Losey, and J. D. Martin, *J. Phys. Chem. B*, **126**, 2265 (2022).
41. S. Khalid, N. Pianta, P. Mustarelli, and R. Ruffo, *Batteries*, **9**, 47 (2023).
42. L. Zhang, I. A. Rodríguez-Pérez, H. Jiang, C. Zhang, D. P. Leonard, Q. Guo, W. Wang, S. Han, L. Wang, and X. Ji, *Adv. Funct. Mater.*, **29**, 1902653 (2019).
43. X. Ji, C. Zhang, H. Jiang, X. Wu, J. Hong, and Y. Xu, *ECS Trans.*, **MA2020-01**, 1431 (2020).
44. X. Zhong, F. Wang, Y. Ding, L. Duan, F. Shi, and C. Wang, *J. Electroanal. Chem.*, **867**, 114193 (2020).
45. X. Wu, Y. Xu, C. Zhang, D. P. Leonard, A. Markir, J. Lu, and X. Ji, *J. Am. Chem. Soc.*, **141**, 6338 (2019).
46. T. F. Burton, R. Jommongkol, Y. Zhu, S. Deebansok, K. Chitbankluai, J. Deng, and O. Fontaine, *Current Opinion in Electrochemistry.*, **35**, 101070 (2022).
47. V. L. Martins and R. M. Torresi, *Curr. Opin. Electrochem.*, **21**, 62 (2020).
48. D. Han, T. Sun, R. Zhang, W. Zhang, T. Ma, H. Du, Q. Wang, D. He, S. Zheng, and Z. Tao, *Adv. Funct. Mater.*, **32**, 2209065 (2022).
49. X. Zheng, T. Ahmad, and W. Chen, *Energy Stor. Mater.*, **39**, 365 (2021).
50. S. D. Han, N. N. Rajput, X. Qu, B. Pan, M. He, M. S. Ferrandon, C. Liao, K. A. Persson, and A. K. Burrell, *ACS Appl. Mater. Inter.*, **8**, 3021 (2016).
51. K. Ta, K. A. See, and A. A. Gewirth, *J. Phys. Chem. C*, **122**, 13790 (2018).
52. C. J. Barile, D. J. Slotcavage, J. Hou, M. T. Strand, T. S. Hernandez, and M. D. McGehee, *Joule.*, **1**, 133 (2017).
53. M. T. Strand, C. J. Barile, T. S. Hernandez, T. E. Dayrit, L. Bertoluzzi, D. J. Slotcavage, and M. D. McGehee, *ACS Energy Lett.*, **3**, 2823 (2018).
54. W. Zheng, *ACS Energy Lett.*, **8**, 1952 (2023).
55. A. L. Yeang, T. S. Hernandez, M. T. Strand, D. J. Slotcavage, E. Abraham, I. I. Smalyukh, C. J. Barile, and M. D. McGehee, *Adv. Energy Mater.*, **12**, 2200854 (2022).
56. M. McEldrew, Z. A. H. Goodwin, S. Bi, A. A. Kornyshev, and M. Z. Bazant, *J. Electrochem. Soc.*, **168**, 050514 (2021).
57. Z. Huang, Z. Li, Y. Wang, J. Cong, X. Wu, X. Song, Y. Ma, H. Xiang, and Y. Huang, *ACS Energy Lett.*, **8**, 372 (2023).
58. W. Du, J. Yan, C. Cao, and C. C. Li, *Energy Stor. Mater.*, **52**, 329 (2022).
59. C. Zhang et al., *Chem. Commun.*, **54**, 14097 (2018).
60. M. Amiri and D. Bélanger, *ChemElectroChem.*, **8**, 2737 (2021).
61. S. Chen, R. Lan, J. Humphreys, and S. Tao, *Energy Stor. Mater.*, **28**, 205 (2020).
62. J. D. Benck, B. A. Pinaud, Y. Gorlin, and T. F. Jaramillo, *PLoS One*, **9**, e107942 (2014).
63. R. Zhao, H. Wang, H. Du, Y. Yang, Z. Gao, L. Qie, and Y. Huang, *Nat. Commun.*, **13**, 3252 (2022).
64. T. Tang et al., *J. Am. Chem. Soc.*, **142**, 7116 (2020).
65. L. Guo, G. Oskam, A. Radisic, P. M. Hoffmann, and P. C. Searson, *J. Phys. D: Appl. Phys.*, **44**, 443001 (2011).
66. M. Qasim, M. Mumtaz, K. Nadeem, and S. Q. Abbas, *J. Nanomater.*, **2016**, 9781790 (2016).
67. S. Mandal and P. K. Samanta, *Mater. Today- Proc.*, **43**, 3091 (2021).
68. S. Ullah, A. Badshah, F. Ahmed, R. Raza, A. Altaf, and R. Hussain, *Int. J. Electrochem.*, **6**, 3801 (2011).
69. C. M. Pelicano, M. D. Balela, and Z. Lockman, *Adv. Mater. Res.*, **1043**, 22 (2014).
70. S. D. Pu et al., *Adv. Mater.*, **34**, 2202552 (2022).